Eur. Phys. J. B (2018) 91: 32
https://doi.org/10.1140/epjb/e2017-80280-7

THE EUROPEAN PHYSICAL JOURNAL B

Regular Article

Computational investigation of CO adsorbed on Au_x, Ag_x and $(AuAg)_x$ nanoclusters (x = 1−5, 147) and monometallic Au and Ag low-energy surfaces[⋆,⋆⋆]

Anna L. Gould[1,2], C. Richard A. Catlow[1,2,3], and Andrew J. Logsdail[1,3,a]

[1] University College London, Kathleen Lonsdale Materials Chemistry, Department of Chemistry, 20 Gordon Street, London WC1H 0AJ, UK
[2] The U.K. Catalysis Hub, Research Complex at Harwell, Rutherford Appleton Laboratory, Oxfordshire OX11 0FA, UK
[3] Cardiff Catalysis Institute, School of Chemistry, Cardiff University, Cardiff CF10 3AT, UK

Received 17 May 2017 / Received in final form 10 July 2017
Published online 12 February 2018

Abstract. Density functional theory calculations have been performed to investigate the use of CO as a probe molecule for the determination of the structure and composition of Au, Ag and AuAg nanoparticles. For very small nanoclusters ($x = 1-5$), the CO vibrational frequencies can be directly correlated to CO adsorption strength, whereas larger 147-atom nanoparticles show a strong energetic preference for CO adsorption at a vertex position but the highest wavenumbers are for the bridge positions. We also studied CO adsorption on Au and Ag (100) and (111) surfaces, for a 1 monolayer coverage, which proves to be energetically favourable on atop only and bridge positions for Au (100) and atop for Ag (100); vibrational frequencies of the CO molecules red-shift to lower wavenumbers as a result of increased metal coordination. We conclude that CO vibrational frequencies cannot be solely relied upon in order to obtain accurate compositional analysis, but we do propose that elemental rearrangement in the core@shell nanoclusters, from Ag@Au (or Au@Ag) to an alloy, would result in a shift in the CO vibrational frequencies that indicate changes in the surface composition.

1 Introduction

Gold nanoclusters (radius < 5 nm) dispersed on metal oxide surfaces have been shown to exhibit surprisingly high catalytic activity and/or selectivity for low-temperature catalytic combustion, partial oxidation of hydrocarbons, hydrogenation of unsaturated hydrocarbons, and reduction of nitrogen oxides [1]. The catalytic activity of the nanoclusters is dependent on the chosen support, preparation method, and the size of the Au nanoclusters [2]. However, accurately identifying the geometry of the reactive nanoparticles remains very difficult due to the multitude of possible structures and dynamic nature of any catalytic system. Furthermore, the complexity is then exacerbated by the interest in alloying of Au with secondary metals to improve economic viability, either through cost reduction or catalytic improvements.

One commonly used method to characterize the electronic and geometric properties of materials is the adsorption of CO, followed by the measurement of infra-red (IR) absorption spectra whereby the changes in the CO molecule's signature frequency can be observed [3–6]. The bonding model for CO to a transition metal, M, involves two components: (1) a donation of the lone pair on C from the 5σ orbital to the vacant metal d orbital ($M \leftarrow$ CO), accompanied by (2) π back donation from the (now filled) metal d-orbital to the empty anti-bonding $2\pi^*$ molecular orbital ($M \rightarrow$ CO). This bonding is synergistic – the more σ donation by the CO ligand, the more electron rich the metal will become, resulting in stronger the π back-bonding. Conversely, if the CO bond is weakened, it lengthens and a shift is observed in the stretching frequency when compared to the gas-phase molecule. Typical stretching frequencies obtained are: gas-phase CO: 2143 cm^{-1}; terminal M−CO: 2125–1850 cm^{-1}; doubly bridged (M_2-CO): 1850–1750 cm^{-1}; triply bridged (M_3-CO): 1675–1600 cm^{-1} [7,8]. The CO stretching frequency is also responsive to the charge on M: each additional

⋆ Contribution to the Topical Issue "Shaping Nanocatalysts", edited by Francesca Baletto, Roy L. Johnston, Jochen Blumberger and Alex Shluger.
⋆⋆ Supplementary material in the form of one pdf file available from the Journal web page at
https://doi.org/10.1140/epjb/e2017-80280-7
[a] e-mail: LogsdailA@cardiff.ac.uk

electron corresponds to a decrease in the wavenumber by approximately 100 cm^{-1}; furthermore, the better the σ-donating (or worse the π-accepting) nature of the other ligands on M, the lower the CO stretching frequency. Therefore, the IR spectra of carbonyl complexes show convenient trends that make CO a useful probe molecule.

Depending on the metallic element, CO can adsorb in an associative or dissociative manner [9–11]. The reactive metals on the left-hand side of the periodic table favour exothermic dissociative adsorption (e.g. Fischer-Tropsch process) [11], which leads to the formation of adsorbed C and O atoms (surface oxide and oxy-carbide compounds); the dissociation barriers are as low as 0.06 eV for Fe(111) [12]. In contrast, the metals on the right-hand side of the d-block (e.g. Pd, Pt, Cu, Ag, Au) interact predominantly in a molecular fashion; the strength of the $M-CO$ bond is much weaker, allowing easy desorption of the CO molecule (without any dissociation) by raising the surface temperature [9,11]. The highest occupied molecular orbital (HOMO), 5σ, is slightly antibonding and has significant C $2s$ character, which is why CO bonds to a metal through the C atom, as a σ-donor, and not the O atom. The lowest unoccupied molecular orbitals (LUMO) are two 2π antibonding orbitals: these interact with metal d-orbitals, accepting electron density. When M is Au, the $5d$ orbitals are filled and below the singly-occupied $6s$ state, thus their involvement in the Au-CO bond is likely to be weak. The major component of the interaction is electrostatic, involving the small $C^{\delta-}{=}O^{\delta+}$ dipole, which can be enhanced through interaction with a cationic Au centre. Thus, Au^- or Au^0 adsorb CO relatively weakly, but Au^+ increases the bond polarisation in the CO molecule, which results in a red-shift (decrease) of the wavenumber for the CO stretching frequency [6,13,14].

The binding of CO to Au_x clusters ($x = 1{-}6$) was previously computationally investigated by Wu et al. [15] using the lowest energy structural isomer for each nuclearity: The most energetically favourable adsorption sites positioned CO in an atop fashion, through a single Au-CO bond, and positively charged clusters had the strongest CO interaction (up to 2.57 eV). As the size of the cluster increased, the difference in the adsorption energies for the varying charge states is reduced, as the additional electrons/holes are distributed over a larger number of atoms. Hybrid density functional theory (Hybrid-DFT) gave lower adsorption energies than standard DFT, by 39–58 kJ mol^{-1}. A similar study by Jiang and Xu [16], also using hybrid-DFT, method showed instead that, for neutral Au_5CO, CO has a lower energy when adsorbed in a bridging position (i.e. bonding to two Au atoms). Recently, computation was with experimental measurements to show that small Au_x nanoclusters are present and catalytically active in the presence of larger nanoparticles; in particular, simulations of Au_5CO produced IR peaks similar to those obtained experimentally by Rogers et al. in their recent experimental investigation [17], which suggests that they observe very small, catalytically-active nanoclusters in their samples. This was later confirmed by aberration-corrected high angle annular dark field scanning transmission electron microscopy (HAADF-STEM) [7].

As cluster size increases ($x > 5$), the difference in adsorption energy for CO on neutral and positively charged clusters again becomes negligible. Molina and Hammer showed that, for Au_{34} clusters, decreasing the coordination number (CN) of an Au atom strengthens CO bonding, and that edge sites assist CO diffusion [18]. In order for CO to adsorb with reasonable cohesion, it was concluded that the coordination number (CN) of the gold atoms must not exceed eight and, under reaction conditions, CO is expected to be highly concentrated at the edges, corners and steps of Au nanoparticles [18]. This has been verified by studies of bulk surfaces, whereby adsorption is most favourable above a surface atom (atop) on the Au (100) and (111) surfaces [19–21].

CO adsorption on Ag/TiO_2 was performed experimentally by Klissurski et al., with the CO stretching frequencies (ν_{C-O}) observed at 2158 and 2165 cm^{-1} assigned to $Ag^+{-}CO$ complexes [22]. However, no carbonyls were formed on Ag following reduction – surface carbonyls with zero-valent Ag atoms do not exist at room temperature [23]. For bulk surfaces, CO adsorption is less favourable on Ag than for Au, with the trend reversing when oxygen is co-adsorbed i.e. CO binds better when the Ag surface has been oxidised. This finding is not unexpected, given the oxidation potential of Ag is smaller than Au at +0.80 and +1.68 eV, respectively [24].

The vulnerability of predicting molecular adsorption on nanoclusters using DFT is well documented: there is a tendency for overestimation of the adsorption energy with high metal coordination. This overestimation stems from the underestimated energy difference between the HOMO (5σ) and LUMO ($2\pi^*$) orbitals in CO, and DFT has been shown to predict the incorrect energetic ordering of CO adsorption for sites on Cu, Rh and Pt [18]. Johnston et al. examined the influence of a dispersion correction for the prediction of adsorption sites on differing precious metal nanoparticles [25,26]. Previously these methods have shown promise for correctly predicting the adsorption of CO on a Pt(111) surface [27,28], but for nanoparticles the dispersion-corrected D3 and D2 functionals, which include an empirical C6 parameter added to the PBE functional [29,30], favoured the (111) face and (111)/(100) edge site on truncated octahedral 38-atom Au nanoparticles, respectively, in contrast to the (100) edge site for PBE and optPBE functionals. CO adsorption on the 55-atom Ih Au nanoparticle also favoured differing sites with different functionals, and significant distortions in the nanoparticle geometry were observed. The ability of adsorbed CO to change the nanoparticle shape can affect the CO stretching frequency, which led the authors to conclude that the use of these dispersion-corrected functionals must be approached with caution. Higher-level theory that implicitly includes dispersion effects, such as the random-phase approximation, has been shown to give improved energetics for CO on Cu(111) surfaces [31], but remains unaffordable for nanoparticles due to the large number of electrons necessary for the simulations.

In this work, we have performed DFT calculations on small M_xCO (M = Ag, Au) clusters to complement and extend our recent work investigating CO on small Au nanoclusters: sub-nanometre particles have very high catalytic activity and greater durability in comparison to larger nanoparticles, and so finding ways to confirm their presence in catalytic materials is important. Here, experimental spectral features are compared with those calculated for Au_{147}, Ag_{147}, Au_{55}@Ag_{92} and Ag_{55}@Au_{92} nanoclusters, which are sizes in the computationally scalable-regime, as well as low-energy Au and Ag surfaces that can be considered representative for thousand-atom nanoparticles and extended bulk-surfaces [32]. The results from these calculations prompt us to ask whether the compositional evolution of core@shell nanoclusters to an alloy can be measured under reaction conditions, with CO used as a probe molecule to determine changes in the nanocluster surface composition.

2 Methodology

2.1 Computational Simulations

DFT calculations were performed using the grid-based projector-augmented wave method (GPAW), with the wavefunctions transformed at the core to a smooth pseudo-wavefunction [33,34]. Converged real-space grid spacings of h = 0.18 Å were used to represent wavefunctions numerically. The frozen-core approximation is used throughout, in keeping with the PAW implementation, with only the valence electrons explicitly included in the calculations: $5d^{10}6s^1$, $4d^{10}5s^1$, $2s^22p^4$ and $2s^22p^2$ states for Au, Ag, O and C, respectively. The generalized gradient approximation (GGA) of Perdew, Burke and Ernzerhof (PBE) was used as the exchange–correlation (XC) functional [35], with dispersion corrections not used due to: (i) the uncertainty of the validity of DFT+D for nanoparticles, specifically due to the risk of erroneous structures [26], and (ii) the large nanoparticle sizes studied making hybrid-DFT unaffordable. The residual minimisation method, direct inversion in iterative subspace (RMM-DIIS) is used to assist convergence of the self-consistent field (SCF) cycle. Geometry optimization convergence was achieved when the forces on all atoms were > 0.01 eV Å^{-1}. For the calculation of vibrational frequencies, the finite-difference method, using a displacement of 0.01 Å, was used to approximate the Hessian force matrix [36].

Geometries of small M_xCO nanoclusters (M = Au, Ag) were taken from the work of Jiang and Xu [16]; Specifically, the geometries of Au_5CO, Au_4CO, Au_3CO, Au_2CO, $Au_2(CO)_2$, $Au(CO)_2$, and AuCO were used. For models with an odd number of metal atoms (x = 1, 3, 5), i.e. those with unpaired electrons, spin-polarized calculations have been used to allow determination of the ground spin-state (μ); for structures with an even number of metal atoms (x = 2, 4), only spin-paired calculations were performed. 147-atom truncated-octahedral nanoclusters were used as a model for nanoparticles in the scalable-regime, as they allow investigation of CO adsorption on both (111) and (100) surfaces with an equal footing. The truncated-octahedron geometries were mathematically constructed [37] and the CO probe molecule positioned at the vertex, edge and hollow surface sites of interest. Slab surface models were realised as an infinite 2-D thin film oriented to expose the facet of interest. The slabs were 5 atomic layers thick, which has previously proven sufficient for surface energy and molecular adsorption energies with converged accuracy [38–40]. Periodic boundary conditions were enforced only in the x- and y-axes, i.e. parallel to the surface, thus removing the need for a dipole correction and preventing periodic interactions between the slab surfaces; **k**-point sampling of reciprocal spaces was performed as one point per 0.024 Å^{-1} in the directions parallel to the slab surface. The CO adsorption on the slabs corresponds to 1 monolayer (ML) at atop, bridge and hollow surface sites on the (100) and (111) faces i.e. high CO partial pressure.

2.2 Energetic analysis

Comparison of the CO binding strength at different adsorption sites is performed by calculating the adsorption energy per CO molecule, E_{ads} (CO), for any given configuration:

$$E_{ads}\,(\mathrm{CO}) = \frac{1}{N_{\mathrm{CO}}}\left(E^{DFT}_{SUP+\mathrm{CO}} - E^{DFT}_{SUP}\right) - E^{DFT}_{\mathrm{CO(g)}}, \quad (1)$$

where N_{CO} is the number of adsorbed CO molecules, $E^{DFT}_{SUP+\mathrm{CO}}$ is the energy of the support with the CO molecules adsorbed, E^{DFT}_{SUP} is the energy of the clean support, and $E^{DFT}_{\mathrm{CO(g)}}$ is the DFT energy of the gas-phase CO molecule. E_{ads} (CO) is referred to henceforth as E_{ads}, with more negative value representing stronger CO bonding.

3 Results

3.1 Small nanoclusters (x ≤ 5)

3.1.1 Adsorption energies

E_{ads} was initially calculated for small Au_xCO and Ag_xCO nanoclusters (Tab. 1); Figure 1 shows the obtained geometries for the Ag_xCO nanoclusters. For odd-electron systems, the influence of spin state has been tested for Au_xCO (Supplementary Information, Table S1); the lowest energy electronic configuration for these clusters occurs when $\mu = 1$, showing that explicit consideration of μ is necessary. CO adsorption is exothermic for all nanoclusters. For Au_xCO, E_{ads} increases with nanocluster size up to $x = 3$, where E_{ads} is at its greatest (–1.808 eV): the two Au atoms not directly bonded to the CO molecule contribute charge transfer to the Au atom that is connected *directly* to CO, as noted by Bader analysis, thus leading to the formation of a stronger σ bond. E_{ads} decreases for $x = 4$ and 5; for Au_5CO ($E_{ads} = -1.200$ eV), Bader analysis shows that the increased number of Au atoms allows for charge delocalisation over the whole nanocluster.

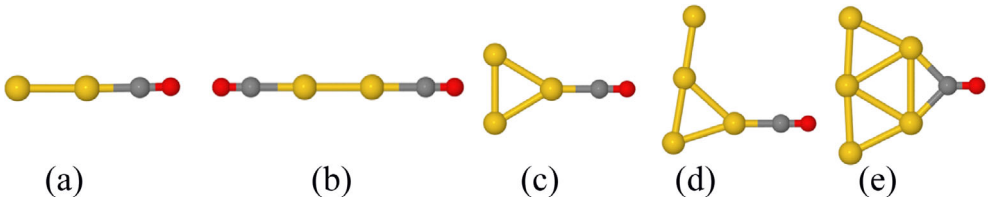

Fig. 1. CO adsorption on small M_xCO nanoclusters ($x \leq 5$), with initial geometries (subsequently reoptimised) taken from Jiang and Xu [16]. Yellow, grey and red spheres represent gold, carbon, and oxygen, respectively.

Table 1. E_{ads} per CO molecule, in eV, for small $M_x(CO)_y$ nanoclusters (M = Au, Ag; $x \leq 5$; $y \leq 2$).

Structure	Spin state (μ)	M = Au	M = Ag
M_5CO	1	−1.200	−0.404
M_4CO	0	−1.746	−1.111
M_3CO	1	−1.808	−0.861
M_2CO	0	−1.673	−0.534
$M_2(CO)_2$	0	−1.322	−0.456
$M(CO)_2$	1	−1.030	−0.514
MCO	1	−0.909	−0.326

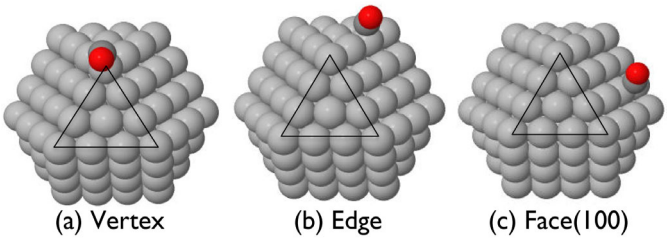

Fig. 2. Adsorption sites for 147-atom nanoparticle, as demonstrated for Ag_{147} (silver), with the (111) face highlighted using a black triangle. CO is positioned on the: (a) vertex; (b) edge; and (c) (100) face sites, with the C and O atoms given in dark grey and red, respectively.

3.1.2 Vibrational frequencies

Using the optimized geometries from Section 3.1.1, ν_{C-O} was calculated using two different methods: (a) all atoms *free*, i.e. forces of all atoms included in the Hessian matrix; (b) all atoms *frozen* except those of importance for the CO adsorption, i.e. forces on C, O and directly bonded M atom(s) were sampled. The interest in comparing these two methods is that the latter, (b), offers significant computational advantages over (a): a finite-difference Hessian matrix calculation involves $6N + 1$ energy evaluations, where N is the number of atoms sampled. Table 2 shows that methods (a) and (b) give essentially identical results throughout, which justifies further use of such a "frozen-atom" approximation when calculating vibrational frequencies in larger systems.

Naively, one would assume that E_{ads} correlates with charge transfer: thus, the strengthening of the M–C bond would be countered by lengthening of the C–O bond, which in turn would lead to a decrease in ν_{C-O}. However, such a correlation is not obvious in our results: the lowest ν_{C-O} is for Au_5CO, which has weaker CO bonding than smaller Au_x nanoclusters ($x = 2$–4). An understanding as to why this occurs can be achieved by referring back to Figure 1: the CO molecule is coordinated with two Au atoms for Au_5CO, as opposed to singly coordinated in all smaller nanoclusters, which means that π back donation from the metal d-orbitals can be achieved from two sources instead of one. Additionally, E_{ads} and ν_{C-O} show no correlation for $x = 1$: ν_{C-O} is 1998.7 cm^{-1}, which is red-shifted in comparison to gas-phase CO (2134.6 cm^{-1}), but E_{ads} is the lowest (weakest) of the models sampled (–0.909 eV). Previous computations using hybrid-DFT obtained ν_{C-O} of 2065.9 cm^{-1}, whilst experimental IR measurements give ν_{C-O} = ∼2039 cm^{-1}, perhaps illustrating that the GGA functional is not ideal for this nuclearity; however, the GGA functional does perform well for $x > 1$, compared to hybrid-DFT, when both are referenced against experimental data. These observations can be rationalized thus: ν_{C-O} is lowest when there is direct chemical bonding, specifically CO 5σ-state → M d-orbital, which is the case for $x = 1$ and 5 (AuCO and Au_5CO). In combination with this, E_{ads} increases with greater back-bonding from the M d-orbitals → CO 2π^*-state, which occurs when the number of M atoms around the M-CO bond increases; partial charge transfer to the C atom can be realised in this case, especially when using a non-local XC functional such as PBE. Overall, ν_{C-O} agrees reasonably with previous computational and experimental measurements [16,17].

3.2 Nanoparticles (x = 147)

3.2.1 Adsorption energies

As a model representation of larger nanoparticles in the scalable-regime with crystalline structures, 147-atom truncated octahedral (TO) nanoparticles were constructed and CO adsorption investigated; the TO model is beneficial as it allows investigation of both (111) and (100) surfaces. Due to the uneven number of metal atoms in these models, it was necessary to use spin-polarised calculations ($\mu = 1$) throughout. CO was adsorbed on Ag_{147} and Au_{147} nanoparticles, as well as core@shell chemical configurations of Ag_{55}@Au_{92} and Au_{55}@Ag_{92}, so as to investigate the change of the characteristic energetic properties for bimetallic systems. Four different adsorption sites were tested: vertex, edge, and (100) and (111) surfaces; however, (111) facets were found to be unstable adsorption sites, with the CO molecule migrating in all cases, and thus are not discussed further. The three stable adsorption sites are shown in Figure 2, with corresponding E_{ads} given in Table 3 and plotted in Figure 3.

Table 2. ν_{C-O} as calculated for $M_x(CO)_y$ (M= Au, Ag; $x \leq 5$; $y \leq 2$) when atoms of the nanocluster are free (frozen); in the case of dual CO adsorption, ν_{C-O} is given for each CO molecule separately when the values are not identical. Comparative experiment and calculated frequencies for M = Au are taken from the work of Jiang and Xu [16], with the computed values obtained using hybrid-DFT calculations (B3LYP). Previous literature is unavailable for M = Ag. All values are in cm^{-1}; ν_{C-O} for gas-phase CO is calculated as 2134.6 cm^{-1}.

Structure	M = Au			M = Ag
	This work	Previous experiment[4]	Previous calculations[4]	This work
M_5CO	1869.9 (1868.0)	1852.9	1923.7	1858.6 (1857.6)
M_4CO	2096.1 (2095.7)	2115.9	2198.0	2067.8 (2067.8)
M_3CO	2084.3 (2083.3)	2075.4	2169.2	2038.5 (2039.3)
M_2CO	2108.3 (2108.5)	2131.9	2192.8	2130.4 (2130.4)
$M_2(CO)_2$	2113.5, 2092.5	2110.2	2186.7	2127.8, 2117.4
$M(CO)_2$	2066.5	1916.3	2103.4	2038.3, 1950.5
MCO	1998.7	2039.3	2065.9	1982.4

Table 3. Adsorption energies (E_{ads}) and corresponding CO vibrational frequencies (ν_{C-O}) for Au, Ag, Ag@Au and Au@Ag 147-atom nanoparticles.

Structure	Vertex		Edge		Face(100)	
	E_{ads} (eV)	ν_{C-O} (cm^{-1})	E_{ads}	ν_{C-O}	E_{ads}	ν_{C-O}
Ag_{147}	−0.319	2083.8	−0.295	2083.6	−0.124	2081.9
$Au_{55}@Ag_{92}$	−0.543	2082.5	−0.418	2088.9	−0.337	2074.8
Au_{147}	−0.757	2096.5	−0.498	2114.2	−0.323	2105.4
$Ag_{55}@Au_{92}$	−0.826	2097.3	−0.493	2096.5	−0.324	2099.9

E_{ads} is negative throughout, indicating that CO adsorption is favourable for all chemical orderings, and at all positions, that were considered. The most negative adsorption energies are obtained for vertex sites, where M has the lowest CN (5): the low coordinated atoms have higher d-states than for atoms with a high coordination number, e.g. edges (CN = 7) and surfaces (CN ≥ 8), making them better at interacting with the LUMO of the CO molecule.

CO adsorption is most favourable for nanoclusters with an Au shell, with $Ag_{55}@Au_{92}$ and Au_{147} exhibiting E_{ads} of −0.826 and −0.757 eV for the vertex position, respectively. The other adsorption sites for these two particular nanoclusters are very similar, suggesting that the influence of the 55-atom Ag core is most strongly felt at the (electronegative) vertices. In contrast, E_{ads} is not similar for Ag_{147} and $Au_{55}@Ag_{92}$: the effect of an Au core is much more pronounced, with $Au_{55}@Ag_{92}$ universally exhibiting more favourable E_{ads}. We also note that E_{ads} for (100) facets is degenerate for most nanoclusters, with the exception of Ag_{147}. Previously, we found $Ag_{55}@Au_{92}$ to be the most energetically favourable chemical ordering for $(AuAg)_{147}$ alloys at the DFT level, which we attributed to the ease of charge transfer to Au [41]; our observations here suggest that this charge redistribution it is also important for CO adsorption.

Table 4 shows the $M-C$ and $C-O$ bond distances for these nanoclusters (d_{M-C} and d_{C-O}, respectively), as well as the partial charges for each adsorption site in the starting (pristine) nanoparticle. E_{ads} is greatest for vertex sites on Au_{147} and $Ag_{55}@Au_{92}$ and we now see that these nanoclusters have the shortest M–C bond distances (1.99 and 2.00 Å, respectively) as well as the greatest electron accumulation (Δq = 0.089 and 0.110 e, respectively). Therefore, a greater amount of charge transfer from the metal to the CO bond occurs, making the CO molecule bond tightly. The vertex sites of Ag_{147} and $Au_{55}@Ag_{92}$ are not as similar: Ag_{147} has the lowest E_{ads} despite greater Δq_{vertex}. At edge sites, Au_{147} and $Ag_{55}@Au_{92}$ have the shortest d_{M-C} and positive Δq values, which indicates that charge accumulation at the surface again leads to short surface bonds to the CO molecule: E_{ads} is almost identical for these two systems, thus demonstrating the dominant roles of these observables in determining favourable adsorption sites. d_{M-C} is very similar for Ag_{147}

Table 4. Bond distances for M–C and C–O (d_{M-C} and d_{C-O}, respectively), in Å, and partial charges (Δq, given in e) according to nanocluster composition and adsorption site.

Site	System	d_{M-C}	d_{C-O}	Δq
Vertex	Au_{147}	1.99	1.15	0.089
	$Ag_{55}@Au_{92}$	2.00	1.15	0.110
	Ag_{147}	2.14	1.14	0.072
	$Au_{55}@Ag_{92}$	2.12	1.14	0.046
Edge	Au_{147}	2.02	1.15	0.022
	$Ag_{55}@Au_{92}$	2.06	1.15	0.079
	Ag_{147}	2.15	1.15	0.007
	$Au_{55}@Ag_{92}$	2.14	1.15	−0.055
Face(100)	Au_{147}	2.05	1.14	0.017
	$Ag_{55}@Au_{92}$	2.13	1.14	0.062
	Ag_{147}	2.19	1.14	0.014
	$Au_{55}@Ag_{92}$	2.16	1.15	−0.07

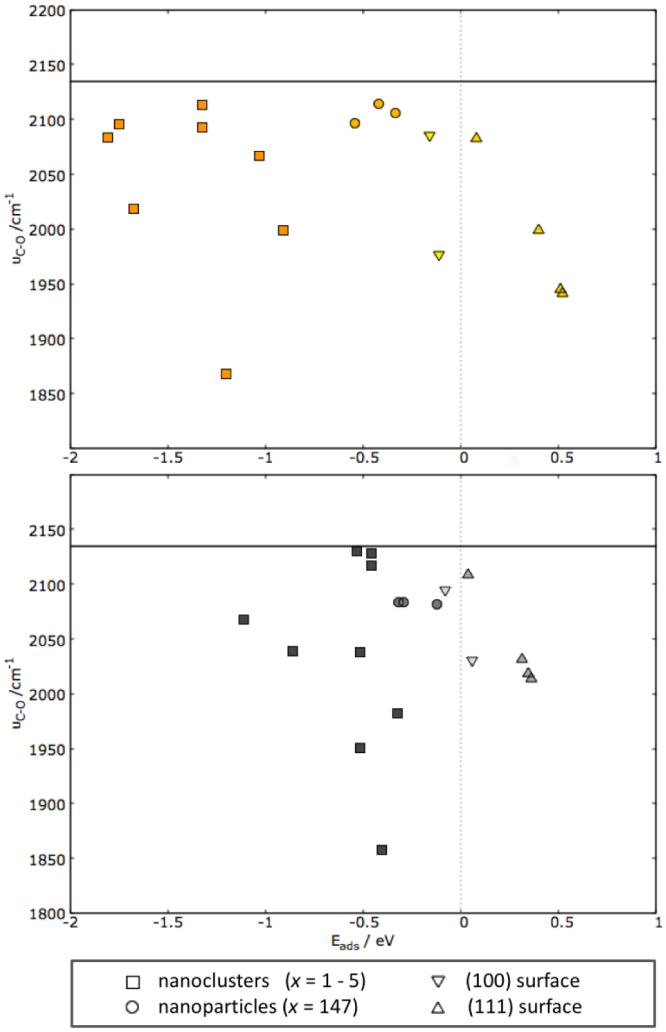

Fig. 3. Graphs of E_{ads} (eV) against ν_{C-O} (cm^{-1}) as calculated for Au (top, golden symbols) and Ag (bottom, silver symbols). Square, circular, down- and up-triangles represent nanoclusters ($x \leq 5$), nanoparticles ($x = 147$), (100) and (111) surfaces, respectively. The reference value of ν_{C-O} calculated in gas-phase for CO is 2134.6 cm^{-1}, and given as solid horizontal black line.

and Au_{55}@Ag_{92}, with the edge site of Au_{55}@Ag_{92} being charge depleted. For CO adsorption on the (100) faces, Au_{147} has the shortest d_{M-C} value (2.05 Å), whereas all other nanoclusters have $d_{M-C} \geq 2.13$ Å. E_{ads} is ∼–0.3 eV for all nanoclusters, with the exception of Ag_{147}, which has the smallest E_{ads} at −0.124 eV; d_{M-C} is also greatest for Ag_{147}. Nonetheless, Au_{147} has a similar E_{ads} to both Au_{55}@Ag_{92} and Ag_{55}@Au_{92}. We suggest that for Au_{55}@Ag_{92}, the electron depleted Ag shell draws greater electron density from the CO molecule. However, rather than completing π-back donation, some of this electron density is lost to the Au-core, resulting in both a longer C−O bond (1.15 Å) and shorter M–C bond (2.16 Å) in comparison to Ag_{147}. Therefore, we suggest that the facet sites can actually *draw* electron density from the CO molecule, resulting in a stronger M−C bond.

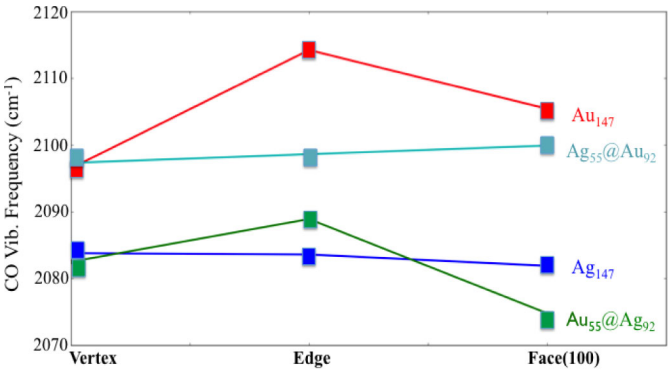

Fig. 4. CO stretching frequency as a function of adsorption site. A description of the colour scheme is given on the graph, with lines given to guide the eye.

3.2.2 Vibrational frequencies

Given the high accuracy achieved in Section 3.1.2 when freezing atoms that are not involved in the M-CO bond, the same localized Hessian has been calculated for the vibrational frequencies of CO on 147-atom nanoparticles. Calculated vibrational frequencies are given in Table 3 and visually represented in Figure 4. We can see that ν_{C-O} generally reflects whether Au or Ag is at the surface: ν_{C-O} of Ag_{55}@Au_{92} is roughly equal to that of Au_{147}, and similarly ν_{C-O} for Au_{55}@Ag_{92} is similar to Ag_{147}. Thus, it is reasonable to assume the IR spectroscopy could be used to identify whether nanoparticles have an Au- or Ag-rich surface, with a separating wavenumber being 2090 cm^{-1}; We tentatively postulate that this observation could be consistent for other geometric motifs with the same elemental configuration, given that the coordination number of vertex, edge and surface atoms does not change. The energetic ordering of sites for E_{ads} is vertex > edge > (100) facet; however, Figure 4 shows that there is an unexpected blue-shift in ν_{C-O} to higher wavenumbers for the edge positions when the nanoparticle has an Au core (Au_{147} and Au_{55}@Ag_{92}); Bader analysis will be pursued and discussed in future work, as CO adsorption could be causing a re-organisation of electron density distribution in the nanoparticle [42].

3.3 Extended surfaces

3.3.1 Adsorption energies

E_{ads} was calculated for 1 monolayer (1 ML) coverage of CO on Au and Ag (100) and (111) surfaces. 1 ML coverage is comparable to high CO partial pressures, and gives a limit to our CO adsorption energies in our investigation. The adsorption sites were equivalent to those tested for the 147-atom nanoparticles: atop, bridge and available hollow sites, which includes both hexagonal close packed (HCP) and face-centred cubic (FCC) on the (111) surface (Fig. 5). Our results are given in Table 5, with E_{ads} most favourable for an atop position on Au (100), at −0.160 eV;

Table 5. CO adsorption energy (E_{ads}) and molecule vibrational frequency (ν_{C-O}), in eV and cm^{-1}, respectively, for different surfaces and adsorption sites. Previously calculated values of E_{ads} are also given.

Surface	Adsorption site	E_{ads}			ν_{C-O}
		This work	Previous calculations		This work
		1 ML	1 ML	≤0.25 ML	1 ML
Au (100)	Atop	−0.160	−0.1[a]	−0.46[b]	2085.4
	Bridge	−0.112	–	−0.55[b]	1976.7
	Hollow	N/A	–	–	N/A
Au (111)	Atop	0.077	–	−0.16[b]	2082.6
	Bridge	0.396	–	−0.15[b]	1998.7
	Hollow (HCP)	0.508	–	−0.16[b]	1941.1
	Hollow (FCC)	0.520	–	−0.12[b]	1944.9
Ag (100)	Atop	−0.083	–	0.19[c]	2094.2
	Bridge	0.055	–	0.13[c]	2030.5
	Hollow	N/A	–	0.14[c]	N/A
Ag (111)	Atop	0.035	–	0.07[d]	2109.0
	Bridge	0.315	–	0.32[d]	2031.4
	Hollow (HCP)	0.345	–	0.36[d]	2013.9
	Hollow (FCC)	0.358	–	0.36[d]	2018.7

[a] 1 ML on 4 layer slab [44]. [b] 0.25 ML coverage, 5 layer slab and 7 layers vacuum; no clear preference for adsorption site. Have a value for hollow site on Au(100) despite also stating that this is not stable [43]. [c] Single CO molecule on cluster model of Ag(100) [46]. [d] 0.25 ML on 4 layer slab, RPBE [21].

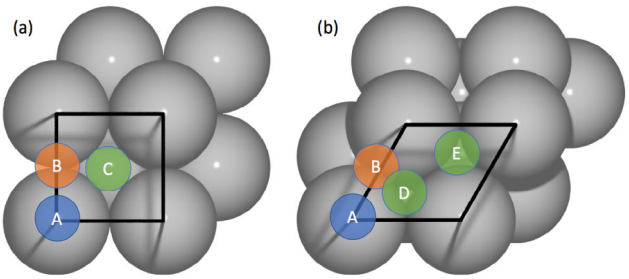

Fig. 5. Different adsorption sites for CO on Ag (100) and (111) surfaces. For (a), the (100) surface: A: atop; B: bridge; C: hollow. For (b), the (111) surface: A: atop; B: bridge; D: FCC hollow; E: HCP hollow. Blue, orange and green spheres correspond to atop, bridge and hollow sites, respectively.

however, the majority of positions on other surfaces are energetically unfavourable, and the (100) hollow was unstable throughout. Previous literature for the adsorption energy of CO on Au surfaces is also given in Table 5 [43,44]: Mehmood et al. obtained a similar result to ourselves, also using a 1 ML coverage, whilst Hussain and co-workers examined a 0.25 ML coverage and showed that CO bonding was exothermic for both (100) and (111) surfaces, i.e. stronger at lower partial pressures, though the energetic ordering of sites is different from our results [43].

3.3.2 Vibrational frequencies

As with our prior work, only directly bonded M atoms are included in the finite difference calculations for determining ν_{C-O}, (Tab. 5). ν_{C-O} for atop adsorption is similar between Au and Ag surfaces, with slightly higher wavenumbers for the Ag surface. For bridged adsorption sites, Au and Ag surfaces can be easily distinguished, with vibrational frequencies occurring at ∼1999 and ∼1977 cm^{-1} for Au and ∼2030 cm^{-1} for Ag. For hollow sites, ν_{C-O} is 1941.1 cm^{-1} and 1944.9 cm^{-1} over the HCP and FCC sites on the Au surface, respectively, whereas it is ∼70 cm^{-1} higher over the same sites on the Ag surface. Overall, ν_{C-O} is inversely correlated with E_{ads}: the C–O bond weakens as the C atom is coordinated with more M atoms.

4 Conclusion

We have performed theoretical calculations to determine whether CO could be used as a probe molecule for determining nanocluster structure and composition. For very small nanoclusters ($x = 1$–5), ν_{C-O} could be directly correlated to the strength of E_{ads}, although agreement for ν_{C-O} between theory and experiment was best for $n \geq 3$. Larger 147-atom nanoparticles showed a strong energetic preference for CO adsorption at a vertex position, followed by edge and face sites. This is attributed to charge accumulation at the vertex sites; however, ν_{C-O} at the Au surfaces cannot be directly correlated to E_{ads}, nor increased coordination, as the bridge positions have the highest calculated wavenumbers. Further work is on-going to see if the nanoparticle geometry, and thus the ratio of (111) and (100) surfaces [31], will affect this observation.

We also studied CO adsorption on Au and Ag (100) and (111) bulk surfaces, for a 1 monolayer coverage. CO adsorption is energetically favourable only on atop and bridge positions for Au (100), and atop for Ag (100). In the case of these surface models, ν_{C-O} red-shifts to

lower wavenumbers with increasing metal coordination. Therefore (in future work), it would be of interest to perform Bader analysis on the surface-adsorbed CO as this may provide insight into the correlation between E_{ads} and ν_{C-O}. Additionally, future work on larger systems should also consider the inclusion of dispersion effects: Baletto et al. showed for Au_{38} and Au_{55} that long-range corrections can have large effects on the underlying nanoparticle structure, but this is dependent on the initial geometry [26]. The influence of dispersion effects on Ag nanoparticles is unknown, and it would be of interest to see its role in AuAg nanoparticles.

Relating the theoretical calculations to experimental work, there is an agreement that an evolution of a greater concentration of Au at the surface will result in a shift in ν_{C-O} to higher wavenumbers. However, the blue shift that is observed experimentally is also a possible indication of nanoparticle oxidation and/or an increase in nanoparticle size. DFT also shows that as the bulk limit is approached, the same generalisations cannot be made, as Ag surfaces actually have a higher wavenumber. Whilst vibrational frequencies cannot be relied upon in terms of compositional analysis, should restructuring of the chemical arrangement of the nanocluster from Ag@Au (or Au@Ag) to an alloy occur, a shift in the vibrational frequencies would indicate a change in the surface composition. Therefore, future experimental studies of AuAg chemical arrangement evolution should strongly consider the importance of nanoparticle structure, as well as CO coverage.

The authors are grateful to Nikolaos Dimitratos for discussions associated with this work. A.L.G. acknowledges the Molecular Modelling and Materials Science Industrial Doctorate Centre (M3S IDC) and Diamond Light Source for funding. A.J.L. acknowledges the Ramsay Memorial Trust and University College London for the provision of a Ramsay Memorial Fellowship. The authors acknowledge the use of the UCL and ARCHER high-performance computing facilities, and associated support services, with the latter supported via their membership of the UK HPC Materials Chemistry Consortium (EP/L000202).

Author contribution statement

All authors contributed to the planning of the simulations. A.L.G. prepared and performed the computational simulations. All authors contributed to the data analysis and preparation of the manuscript.

References

1. M. Haruta, Catal. Today **36**, 153 (1997)
2. M. Valden, X. Lai, D.W. Goodman, Science **281**, 1647 (1998)
3. G. Blyholder, J. Phys. Chem. **68**, 2772 (1964)
4. A. Fielicke, G. von Helden, G. Meijer, B. Simard, D.M. Rayner, J. Phys. Chem. B **109**, 23935 (2005)
5. W.-L. Lim, T. Nowitzki, M. Necke, H. Schnars, P. Nickut, J. Biener, M.M. Biener, V. Zielasek, K. Al-Shamery, T. Klüner, M. Baumer, J. Phys. Chem. C **111**, 445 (2007)
6. J. Velasquez, III, B. Njegic, M.S. Gordon, M.A. Duncan, J. Phys. Chem. A **112**, 1907 (2008)
7. P. Atkins, *Shriver and Atkins' inorganic chemistry* (Oxford University Press, USA, 2010)
8. C.E. Housecroft, A.G. Sharpe, *Inorganic Chemistry* (Prentice Hall, 2005)
9. I. Chorkendorff, J. Niemantsverdriet, *Concepts of Modern Catalysis and Kinetics* (Wiley-VCH, Germany, 2013)
10. B. Hammer, Y. Morikawa, J.K. Nørskov, Phys. Rev. Lett. **76**, 2141 (1996)
11. J.K. Nørskov, T. Bligaard, J. Rossmeisl, C.H. Christensen, Nat. Chem. **1**, 37 (2009)
12. T. Wang, X.-X. Tian, Y.-W. Li, J. Wang, M. Beller, H. Jiao, ACS Catal. **4**, 1991 (2014)
13. A.J. Lupinetti, S. Fau, G. Frenking, S.H. Strauss, J. Phys. Chem. A **101**, (1997) 9551
14. X. Wu, L. Senapati, S.K. Nayak, J. Phys. Chem. **117**, 4010 (2002)
15. X. Wu, L. Senapati, S. Nayak, A. Selloni, M. Hajaligol, J. Phys. Chem. **117**, 4010 (2002)
16. L. Jiang, Q. Xu, J. Phys. Chem. A **109**, 1026 (2005)
17. S.M. Rogers, C.R.A. Catlow, C.E. Chan-Thaw, D. Gianolio, E.K. Gibson, A.L. Gould, N. Jian, A.J. Logsdail, R.E. Palmer, L. Prati, N. Dimitratos, A. Villa, P.P. Wells, ACS Catal. **5**, 4377 (2015)
18. L. Molina, B. Hammer, Appl. Catal. A: Gen. **291**, 21 (2005)
19. M. Gajdoš, A. Eichler, J. Hafner, J. Phys.: Condens. Matter **16**, 1141 (2004)
20. B. Hammer, Y. Morikawa, J.K. Norskov, Phys. Rev. Lett. **76**, 2141 (1996)
21. F. Abild-Pedersen, M. Andersson, Surf. Sci. **601**, 1747 (2007)
22. K. Hadjiivanov, E. Vasileva, M. Kantcheva, D. Klissurski, Mater. Chem. Phys. **28**, 367 (1991)
23. K.I. Hadjiivanov, G.N. Vayssilov, Adv. Catal. **47**, 307 (2002)
24. D.D. Ebbing, General Chemistry, 3rd ed. (Houghton Mifflin, 1990)
25. L.O. Paz-Borbon, R. Johnston, G. Barcaro, A. Fortunelli, Eur. Phys. J. D **52**, 131 (2009)
26. J.B. Davis, F. Baletto, R.L. Johnston, J. Phys. Chem. A **119**, 9703 (2015)
27. M. Dion, H. Rydberg, E. Schröder, D.C. Langreth, B.I. Lundqvist, Phys. Rev. Lett. **92**, 246401 (2004)
28. P. Laziæ, M. Alaei, N. Atodiresei, V. Caciuc, R. Brako, S. Blügel, Phys. Rev. B **81**, 045401 (2010)
29. S. Grimme, J. Comput. Chem. **27**, 1787 (2006)
30. S. Grimme, J. Antony, S. Ehrlich, S. Krieg, J. Chem. Phys. **132**, 154104 (2010)
31. X. Ren, P. Rinke, M. Scheffler, Phys. Rev. B **80**, 045402 (2009)

32. F. Viñes, J.R.B. Gomes, F. Illas, Chem. Soc. Rev. **43**, 4922 (2014)
33. P.E. Blöchl, Phys. Rev. B **50**, (1994) 17953
34. J.J. Mortensen, L.B. Hansen, K.W. Jacobsen, Phys. Rev. B **71**, 035109 (2005)
35. J.P. Perdew, K. Burke, M. Ernzerhof, Phys. Rev. Lett. **77**, 3865 (1996)
36. A.H. Larsen, J.J. Mortensen, J. Blomqvist, I.E. Castelli, R. Christensen, M. Dułak, J. Friis, M.N. Groves, B. Hammer, C. Hargus, E.D. Hermes, P.C. Jennings, P.B. Jensen, J. Kermode, J.R. Kitchin, E.L. Kolsbjerg, J. Kubal, K. Kaasbjerg, S. Lysgaard, J.B. Maronsson, T. Maxson, T. Olsen, L. Pastewka, A, Peterson, C. Rostgaard, J. Schiøtz, O. Schütt, M. Strange, K.S. Thygesen, T. Vegge, L. Vilhelmsen, M. Walter, Z. Zeng, K.W. Jacobsen, J. Phys.: Condens. Matter **29**, 273002 (2017)
37. A.J. Logsdail, R.L. Johnston, RSC Adv. **2**, 5863 (2012)
38. L. Vitosa, A.V. Rubana, H.L. Skrivera, J. Kollárb, Surf. Sci. **411**, 186 (1998)
39. M. Mavrikakis, P. Stoltze, J.K. Nørskov, Catal. Lett. **64**, 101 (2000)
40. F. Abild-Pedersen, J. Greeley, F. Studt, J. Rossmeisl, T.R. Munter, P.G. Moses, E. Skúlason, T. Bligaard, J.K. Nørskov, Phys. Rev. Lett. **99**, 016105 (2007)
41. A.L. Gould, C.J. Heard, A.J. Logsdail, C.R.A. Catlow, Phys. Chem. Chem. Phys. **16**, 21049 (2014)
42. M. Boronat, P. Concepción, A. Corma, J. Phys. Chem. C **113**, 16772 (2009)
43. A. Hussain, D.C. Ferré, J. Gracia, B. Nieuwenhuys, Surf. Sci. **603**, 2734 (2009)
44. F. Mehmood, A. Kara, T.S. Rahman, C.R. Henry, Phys. Rev. B **79**, 075422 (2009)
45. B. Pascucci, G.S. Otero, P.G. Belelli, F. Illas, M.M. Branda, J. Mol. Model. **20**, 2448 (2014)
46. C. Qin, L.S. Sremaniak, J.L. Whitten, J. Phys. Chem. B **110**, 11272 (2006)